Role of an isolated eddy near the turbulent/non-turbulent interface layer

T. Watanabe,[1,2,*] R. Jaulino,[2] R. R. Taveira,[2] C. B. da Silva,[1,2] K. Nagata,[1] and Y. Sakai[3]
[1]*Department of Aerospace Engineering, Nagoya University, 464-8603 Nagoya, Japan*
[2]*LAETA, IDMEC, Instituto Superior Técnico, Universidade de Lisboa, Avenida Rovisco Pais, 1049-001 Lisboa, Portugal*
[3]*Department of Mechanical Science and Engineering, Nagoya University, 464-8603 Nagoya, Japan*
(Received 10 December 2016; published 25 September 2017)

A simple analytical description for the effects of a single vortex near a turbulent/non-turbulent interface (TNTI) layer, based on a Burgers vortex (BV) model, is compared with results from direct numerical simulation (DNS) of shear-free turbulence. The BV model parameters are derived from the DNS data, and the model separates the entrainment as a two-stage process: (i) the strain imposed on the vortex draws non-turbulent fluid toward the irrotational boundary that separates the irrotational from the turbulent region, and afterwards (ii) the velocity associated with the vorticity field moves the entrained fluid toward the turbulent core region. The resulting model is able to predict the enstrophy dynamics, flow streamlines, and flow topology—such as the formation of the teardrop map in the invariants of the velocity gradient tensor—as well as the entrainment velocity. The BV model provides an interesting framework to analyze the small-scale "nibbling" eddy motions near the TNTI and allows the inclusion of the large-scale flow-dependent effects imposed by the strain rate, while it also links the entrainment characteristics to the eddy structure of the flow near TNTIs.

DOI: 10.1103/PhysRevFluids.2.094607

I. INTRODUCTION

In jets, wakes, mixing layers, and boundary layers, a turbulent/non-turbulent interface (TNTI) layer separates the turbulent from the non-turbulent (irrotational) flow. This layer has finite thickness consisting of a turbulent sublayer (TSL) and a viscous superlayer (VSL) [1]. It has been shown that the flow dynamics is quite different inside these two layers: viscous effects prevail over inviscid vortex stretching within the VSL, whereas inviscid processes are important inside the TSL. Understanding how the non-turbulent fluid is entrained across the TNTI layer is crucial in order to predict and control mass, momentum, and scalar transfers in turbulent flows, which are omnipresent in engineering and geophysical flows. The entrainment process has been studied recently with high-resolution direct numerical simulation (DNS) [2–5] and experiments with laser-based measurements [6–9], such as particle image velocimetry. These studies have shown that the entrainment is characterized by a two-stage process with different length scales [8,10]. Initially the non-turbulent fluid acquires vorticity near the outer edge of the TNTI by viscous diffusion [7], and later it is entrained into the turbulent region across the TNTI layer. We denote the initial fluid motion across the outer edge of the TNTI layer as *local entrainment*. Shortly after the local entrainment has taken place, the fluid is transferred toward the turbulent-core region across the TNTI layer.

Despite these studies, the detailed mechanism by which the turbulence structures contribute to the entrainment across the TNTI layer remains unclear. DNS studies have confirmed the existence of small-scale intense vorticity structures near the TNTI [11–13], and in this study we focus on the entrainment process caused by the small-scale motions induced by these structures near the TNTI, often referred to as *nibbling*, rather than on the motions induced by the large-scales eddies, described as *engulfment*, even if these large-scale motions are thought to impose the entrainment

*watanabe.tomoaki@c.nagoya-u.jp

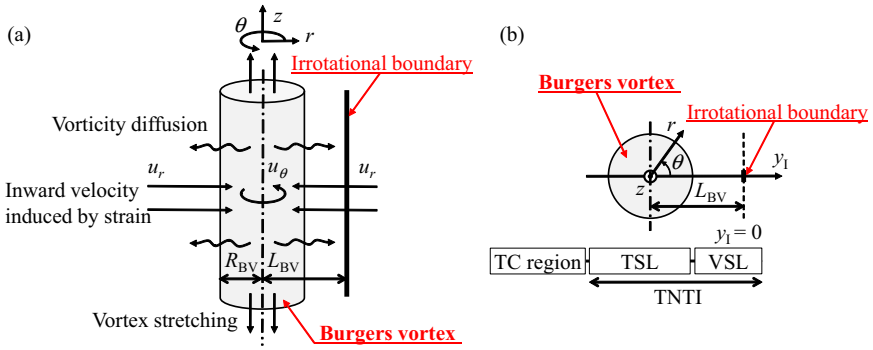

FIG. 1. (a) Definitions used in the entrainment model based on the Burgers vortex, with a (constant) core radius R_{BV}, and its associated tangential u_θ and radial u_r velocities, caused by the balance between vortex stretching and viscous diffusion. (b) The location of the viscous superlayer (VSL), turbulent sublayer (TSL), and the turbulent core (TC) regions, in relation to the irrotational boundary, which is at the outer edge of the TNTI layer at a distance equal to L_{BV} from the vortex center.

rate [14]; i.e., we focus on the small-scale entrainment mechanism, rather than on the imposition of the entrainment rate. Specifically, we analyze the role of an isolated eddy near the TNTI layer and develop a simple model for the entrainment, which is based on the Burgers vortex. The entrainment characteristics derived from this simple model are compared to DNS of shear-free turbulence (SFT) [15].

We show that an isolated eddy described by the Burgers vortex successfully predicts flow characteristics within the TNTI layer, such as a nibbling type of entrainment and the particular behavior of the invariants of the velocity gradient tensor near the TNTI layer, and provides a simple model linking the entrainment characteristics to the small-scale eddies of turbulent flows. The model can be easily extended to include the effects of large-scale eddies, which are found at the edges of jets and mixing layers.

II. ENTRAINMENT CHARACTERISTICS CAUSED BY AN ISOLATED EDDY

In this study, we analyze the entrainment characteristics created by the presence of an isolated eddy near the TNTI layer, which is modeled by a steady Burgers vortex (BV) [16], as illustrated in Fig. 1. The velocity field in a BV, $\mathbf{U}_{\mathrm{BV}} = (u_r, u_\theta, u_z)$, is given by $\mathbf{U}_{\mathrm{BV}} = \mathbf{U}^\alpha + \mathbf{U}^\omega$, where $\mathbf{U}^\alpha$ and $\mathbf{U}^\omega$ are the velocity fields associated with the irrotational strain and vorticity, respectively:

$$\mathbf{U}^\alpha = \left(u_r^\alpha(r), 0, u_z^\alpha(z)\right) = \left(-\frac{1}{2}\alpha r, 0, \alpha z\right), \tag{1}$$

$$\mathbf{U}^\omega = \left(0, u_\theta^\omega(r), 0\right) = \left(0, \frac{\Gamma_0}{2\pi r}\left[1 - \exp\left(-\frac{r^2}{R_{\mathrm{BV}}^2}\right)\right], 0\right). \tag{2}$$

Here, α is the strain acting on the vortex, R_{BV} is the constant radius of the vortex core, and Γ_0 is the circulation. The vorticity vector field, which is the curl of the velocity $\omega_i = \varepsilon_{ijk}\partial u_k/\partial x_j$, is non-zero only for the axial (z) component, which is given by $\omega_z(r) = \omega_0 \exp(-r^2/R_{\mathrm{BV}}^2)$, where $\omega_0 = \omega_z(r=0) = \Gamma_0/\pi R_{\mathrm{BV}}^2$. The radius of the vortex is equal to $R_{\mathrm{BV}} = \sqrt{4\nu/\alpha}$, where ν is the kinematic viscosity. Thus, the BV model has three parameters: Γ_0, α, and ν (or Γ_0, R_{BV}, and ν).

The radial profiles of the enstrophy $\omega^2 = \omega_i\omega_i$, enstrophy production $P_\omega = \omega_i s_{ij} \omega_j$, where $s_{ij} = (\partial u_i/\partial x_j + \partial u_j/\partial x_i)/2$ is the rate-of-strain tensor, and enstrophy diffusion

$D_\omega = \nu\partial^2(\omega_i\omega_i/2)/\partial x_j\partial x_j$ are then given by [17]

$$\omega^2(r) = \omega_0^2 \exp\left(\frac{-2r^2}{R_{\rm BV}^2}\right), \tag{3}$$

$$P_\omega(r) = \omega_0^2\alpha \exp\left(\frac{-2r^2}{R_{\rm BV}^2}\right), \tag{4}$$

and

$$D_\omega(r) = \left(\frac{4\nu\omega_0^2}{R_{\rm BV}^2}\right)\left(\frac{2r^2}{R_{\rm BV}^2} - 1\right)\exp\left(\frac{-2r^2}{R_{\rm BV}^2}\right), \tag{5}$$

respectively. Interestingly, the second and third invariants of the velocity gradient tensor $A_{ij} = \partial u_i/\partial x_j$,

$$Q = \tfrac{1}{4}(\omega_i\omega_i - 2s_{ij}s_{ij}) \tag{6}$$

and

$$R = -\tfrac{1}{3}\left(s_{ij}s_{jk}s_{ki} + \tfrac{3}{4}\omega_i s_{ij}\omega_j\right), \tag{7}$$

respectively, are related by a very simple expression for the Burgers vortex flow, namely,

$$Q = -\frac{R}{\alpha} - \alpha^2, \tag{8}$$

and for instance the radial profile of the second invariant $Q(r)$ is given by [16]

$$Q(r) = \frac{\omega_0^2}{4}(F_\omega(\xi) - F_s(\xi)), \tag{9}$$

where $F_\omega(\xi) = e^{-2\xi}$, $F_s(\xi) = \xi^{-2}[1 - (1+\xi)e^{-\xi}]^2$, and $\xi = r^2/R_{\rm BV}^2$.

The entrainment is here analyzed in relation to a particular position within the TNTI layer—the *irrotational boundary* defined by Watanabe *et al.* [18]—which is the outer edge of the TNTI layer [1], detected as the isosurface of the vorticity magnitude, which separates the turbulent and non-turbulent regions [19]. The flow characteristics within the TNTI layer are very different depending on the sublayer (VSL or TSL). The determination of the outer edge of the TNTI layer, the irrotational boundary (IB) position, enables us to connect the statistics between the two (sub)layers within the TNTI layer. We define $L_{\rm BV}$ as the distance from the axis of the isolated BV to the irrotational boundary (see Fig. 1), while the y_I coordinate points into the non-turbulent region, with the origin located at the irrotational boundary. Figure 1 also represents the typical mechanism associated with the BV, including its balance between vortex stretching and vortex diffusion, its associated (constant) radius $R_{\rm BV}$, and induced tangential u_θ and radial u_r velocities [Fig. 1(a)], as well as the locations of the VSL, TSL, and the turbulent core (TC) regions [Fig. 1(b)].

Since in general the irrotational boundary moves with a given velocity, here denoted by $\mathbf{U}^{\rm I}$, the entrainment characteristics need to be studied with the velocity of the fluid relative to the irrotational boundary movement $\Delta\mathbf{U} = \mathbf{U} - \mathbf{U}^{\rm I}$, where $\mathbf{U}$ is the absolute fluid velocity [20]. Moreover, the relative velocity vector $\Delta\mathbf{U}$ can be decomposed into its normal and tangential components with respect to the irrotational boundary, which are represented by ΔU_N and $\Delta\mathbf{U}_{\rm T} = \Delta\mathbf{U} - \Delta U_N\mathbf{n}$, respectively, where $\Delta U_N = \Delta\mathbf{U}\cdot\mathbf{n}$, and $\mathbf{n} = -\nabla\omega^2/|\nabla\omega^2|$ is the unit normal vector of the irrotational boundary and points into the non-turbulent region. Since the tangential relative velocity component is oriented in an arbitrary direction on the plane perpendicular to $\mathbf{n}$, we use the magnitude of the tangential relative velocity component $\Delta U_T = |\Delta\mathbf{U}_{\rm T}|$. Although the Eulerian statistics of the relative velocity do not show the actual path of the entrained fluid particles, both Lagrangian particle tracking and Eulerian statistics have been shown to display similar movements of the fluid particles during the entrainment [10,18,19].

Finally, the local entrainment velocity v_E, which is the velocity of the fluid across the irrotational boundary, can be computed as the propagation velocity of the enstrophy isosurface $v_E\mathbf{n}$ from the enstrophy transport equation [7]:

$$v_E = \left(\frac{2\omega_i s_{ij} \omega_j}{|\nabla \omega^2|} + \frac{2\nu\omega_i \nabla^2 \omega_i}{|\nabla \omega^2|} \right). \tag{10}$$

It has been shown that v_E is of the order of the Kolmogorov velocity $u_\eta = (\nu\varepsilon)^{1/4}$ (ε is the dissipation rate of turbulent kinetic energy) [21], and positive v_E represents a propagation of the irrotational boundary into the non-turbulent region.

Using the above definitions, we can write the y_I-direction velocity component of $\mathbf{U}^I$ on the y_I axis as $\mathbf{U}^I \cdot \mathbf{n} = v_E + u_r^\alpha(L_{BV})$. For a steady BV, the irrotational boundary does not move in the r direction, i.e., $\mathbf{U}^I \cdot \mathbf{n} = 0$, and therefore, the local entrainment velocity associated with the BV is given by

$$v_E = -u_r^\alpha(L_{BV}) = \tfrac{1}{2}\alpha L_{BV}. \tag{11}$$

The normal and tangential velocities relative to the irrotational boundary can be obtained in the r-θ plane and are given by

$$\Delta U_N(r,\theta) = u_r^\alpha(r)\cos\theta - u_\theta^\omega(r)\sin\theta, \tag{12}$$

$$\Delta U_T(r,\theta) = \left| \left(u_r^\alpha(r)\sin\theta + u_\theta^\omega(r)\cos\theta\right) - u_\theta^\omega(L_{BV}) \right|, \tag{13}$$

respectively, where θ is the angle from the y_I direction [Fig. 1(b)]. On the y_I axis ($\theta = 0$), the relative velocities become

$$\Delta U_N(r) = u_r^\alpha(r), \tag{14}$$

$$\Delta U_T(r) = \left| u_\theta^\omega(r) - u_\theta^\omega(L_{BV}) \right|, \tag{15}$$

and thus ΔU_N and ΔU_T are also related to the strain and vorticity fields, respectively.

Recall that many intense vortex structures (IVSs) have their cores (or central axis) within the TSL. However, any of these vortex axes is hardly to be found inside the VSL because this layer is so thin that it cannot possibly contain IVSs [11]. Thus, the radius of the vortex cores is linked to the distance between the vortex center (or axis) and the boundary between the TSL and VSL. Therefore, since the irrotational boundary is located at the outer edge of the VSL, the distance from the vortex core axis to the irrotational boundary, L_{BV}, can be rigorously defined by

$$L_{BV} = R_{BV} + \delta_\nu, \tag{16}$$

where δ_ν is the VSL thickness. The typical mean VSL thickness is about $\delta_\nu \approx 4\eta$ [12,17], and similarly, the typical vortex core radius observed in various turbulent flows is also $R_{BV} \approx 5\eta$ [22], where $\eta = (\nu^3/\varepsilon)^{1/4}$ is the Kolmogorov microscale. Thus, we can define

$$R_{BV} = C_R\eta \tag{17}$$

and

$$\delta_\nu = C_\delta\eta, \tag{18}$$

where C_R and C_δ are constants of order 1 [2]. Thus, the entrainment velocity based on the BV model includes two new additional parameters: C_R and C_δ. It is noteworthy that the large scales affect the model by the imposition of the strain field (thus by imposing α) as described by Jiménez and Wray [22] (see also Ref. [11]) and, therefore, the present analytical model can be used to describe TNTIs from different flows through the imposition of an appropriate value for α. Finally, it should be noted that the intense vorticity structures have a radius of $\sim 5\eta$ [22]. This indicates that they

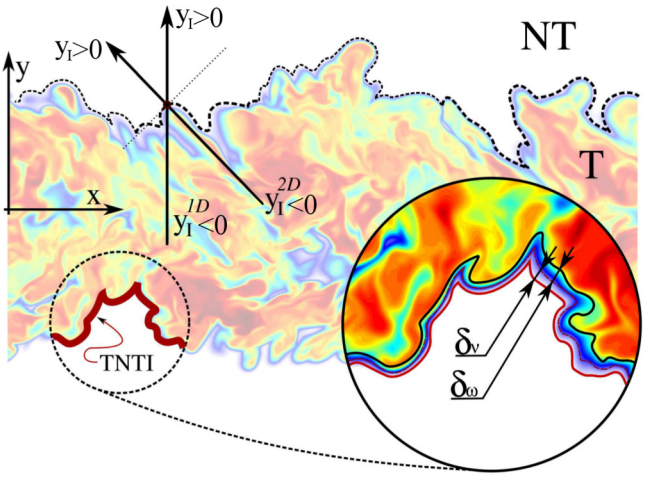

FIG. 2. Local coordinate systems used to compute the conditional mean profiles, in relation to the distance from the irrotational boundary at the outer edge of the TNTI, which separates the turbulent (T) and non-turbulent (NT) flow regions: 1D, along the y direction; 2D, normal to the interface in the (x,y) plane; and 3D, normal to the local interface (not shown). The TNTI comprises two (sub)layers: the viscous superlayer with thickness δ_ν and the turbulent sublayer with thickness δ_ω.

are stretched by the local (fluctuating) strain field, whose magnitude is of the order of $\alpha \sim \langle\omega^2\rangle^{1/2}$ [16,22]. However, even though the stretching is related to the local strain, the intense tubelike vortex structures are long lived and stable compared with vorticity sheets [23].

III. DIRECT NUMERICAL SIMULATIONS OF SHEAR FREE TURBULENCE

DNS of SFT was carried out in a periodic box with sizes 2π with 512^3 collocation points [15] to study the entrainment characteristics in the TNTI and to assess the results obtained with the present model. The DNS code uses pseudospectral methods for spatial discretization and a third-order Runge-Kutta method for temporal advancement. The details on the DNS were described in previous studies [15,17,24], and here these simulations are only briefly described. After an initial DNS of forced homogeneous isotropic turbulence (HIT) has been carried out, the boundary between the turbulent and the non-turbulent flows is generated by instantaneously inserting the HIT into the middle of a quiescent flow. The initial field consists of the HIT around the center of the computational domain ($|y| \leqslant 0.7\pi$) and the non-turbulent flow with zero velocity ($0.7\pi < |y| \leqslant \pi$). After this insertion step, the turbulent (central) region then spreads into the non-turbulent region in the y direction in the absence of mean shear.

The TNTI is investigated using one single instantaneous field from the SFT simulation. The turbulent Reynolds number is $\mathrm{Re}_\lambda = u_{\mathrm{rms}}\lambda_x/\nu = 115$ at the center of the SFT, where u_{rms} is the rms velocity in the x direction and λ_x is the Taylor microscale calculated with the x-direction velocity. The ratio between λ_x and η is $\lambda_x/\eta = 19.5$ at $y = 0$, while the resolution at $y = 0$ is $\Delta x/\eta = 1.5$.

IV. FLOW CHARACTERISTICS IN RELATION TO THE DISTANCE FROM THE TNTI

In this section, we review several conditional statistics (in relation to the TNTI), which have been employed in many recent works [1], and the procedure to obtain them is only briefly described here. The procedure starts with the determination of the irrotational boundary, which is defined by the surface where the vorticity magnitude is equal to a certain threshold ω_{th}, whose precise value is determined by using the dependence of the turbulent volume on ω_{th}, as in Ref. [19]. After the

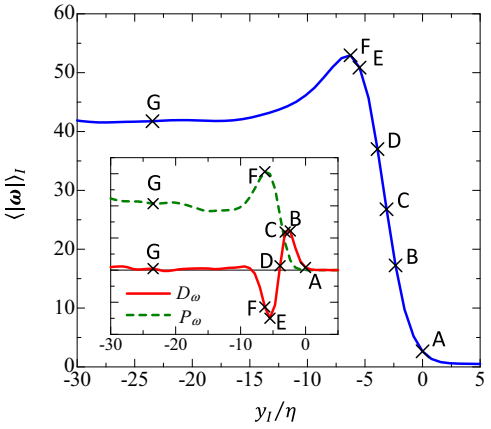

FIG. 3. Conditional mean profiles (as a function of the distance from the irrotational boundary) of vorticity magnitude $|\boldsymbol{\omega}|$, enstrophy production (P_ω), and enstrophy viscous diffusion (D_ω).

determination of the irrotational boundary location, the conditional statistics are computed as a function of the distance to the irrotational boundary y_I. The conditional statistics are computed using one of three possible orientations to the interface (see Fig. 2): (i) "vertical" to the TNTI, i.e., parallel to the y axis (1D), (ii) normal to the TNTI projected into the (x,y) plane (2D), or (iii) normal to the TNTI (3D). For case iii we introduce a local coordinate y_I, whose direction given by $\mathbf{n}$ is locally normal to the irrotational boundary. In the resulting conditional mean profile, the irrotational boundary is by definition located at $y_I = 0$, while the non-turbulent and turbulent regions are defined by $y_I > 0$ and $y_I < 0$, respectively, where y_I is normalized by the Kolmogorov length scale in the turbulent region $\eta = \eta(y_I \ll 0)$. We denote these conditional averages by $\langle\,\rangle_I$. Figure 3 illustrates the enstrophy buildup mechanisms across the TNTI by plotting conditional mean profiles of vorticity magnitude $|\boldsymbol{\omega}|$, enstrophy viscous diffusion D_ω, and enstrophy production P_ω, for the present DNS. Several letters (A–G) are assigned to specific locations within the TNTI (see Table I), where A denotes the irrotational boundary at the start or at the "outer edge" of the TNTI (i.e., the origin of the local reference frame $y_I = 0$). The viscous diffusion exhibits a characteristic shape with positive or negative maxima at $y_I/\eta = -2.4$ (B) and $y_I/\eta = -5.5$ (E) associated with gain or loss of enstrophy, respectively, as previously reported by several authors [1], and it is clear that this is the first mechanism driving the observed enstrophy rise inside the TNTI. The diffusive transport switches signal between the two extrema crossing zero at $y_I/\eta = -3.9$ (D). On the other hand, the enstrophy production starts to be important after $y_I/\eta \approx -2$ and is responsible for the enstrophy amplification for $y_I/\eta \leqslant -3.3$ because at this point the enstrophy production surpasses the viscous diffusion. The conditional mean vorticity magnitude exhibits a sharp rise in the range $-6.3 \leqslant y_I/\eta \leqslant 0$ (A–F) until at $y_I/\eta = -6.3$ (F) the maximum vorticity magnitude is attained. At $y_I/\eta = -23.5$ (G), the flow exhibits all the characteristics of fully developed turbulence, with

TABLE I. Letters used to denote several points across the TNTI layer, which is divided into the viscous superlayer (VSL) and the turbulent sublayer (TSL) [17]. The irrotational boundary (IB) location $y_I = 0$ is also indicated. Point G is deep inside the turbulent-core (TC) region where production and dissipation of enstrophy roughly balance.

Letter	A	B	C	D	E	F	G
(Sub)layer	IB	VSL	VSL	TSL	TSL	TSL	TC
y_I/η	0.0	−2.4	−3.1	−3.9	−5.5	−6.3	−23.5

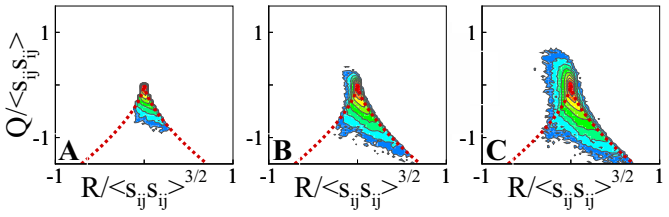

FIG. 4. Joint probability density function of Q and R across the VSL region in the flow: start of the viscous superlayer (irrotational boundary) (A), point of maximum mean enstrophy diffusion (B), and point close to the boundary between the viscous superlayer and the turbulent sublayer (C).

no sign of the presence of the TNTI. Therefore, in the present case the VSL, associated with the viscous diffusion of vorticity toward the non-turbulent flow region, extends from $-3.3 \lesssim y_I/\eta \lesssim 0$ (A, B, and C), i.e., with a mean thickness (defined by the region in Fig. 3 where diffusion exceeds production) equal to $\langle \delta_\nu \rangle \approx 3.3\eta$, while the TSL (associated with the rapid vorticity rise by the enstrophy production) lies in the range $-6.3 \leqslant y_I/\eta \leqslant -3.3$ (D, E, and F), with an estimated mean thickness (region where production exceeds diffusion culminating in the maximum vorticity; Fig. 3) equal to $\langle \delta_\omega \rangle \approx 3\eta$. Thus, in the present flow, both $\langle \delta_\omega \rangle \sim \langle \delta_\nu \rangle \sim \eta$ in agreement with Ref. [17], because the coherent structures consist solely of "worms."

The very different nature of the VSL and TSL can be further appreciated by analyzing the evolution of the invariants Q and R across the TNTI layer, whose values somehow reflect the interplay between strain and vorticity, which is so important in turbulent flows. Recall that the enstrophy is proportional to the vorticity magnitude $|\boldsymbol{\omega}| = (\omega_i \omega_i)^{1/2}$ while the strain is proportional to the viscous dissipation rate of kinetic energy, $\varepsilon = 2\nu s^2$, where $s^2 = s_{ij} s_{ij}$. At high Reynolds numbers strong enstrophy is concentrated in coherent tubelike structures or eddies (worms) with a lifetime comparable to the reference time scale of the flow, whereas regions of strong strain are "incoherent," "short lived," and tend to be a maximum near the periphery of the eddies [16].

If $Q > 0$, enstrophy dominates over strain, and hence $Q \gg 0$ leads to $R \sim -\omega_i \omega_j s_{ij}/4$. Consequently, $R < 0$ shows the predominance of vortex stretching (positive enstrophy production) events over compression, whereas $R > 0$ implies a predominance of vortex compression over stretching. On the other hand, if $Q \ll 0$, $R \sim -s_{ij} s_{jk} s_{ki}/3 = -\alpha_S \beta_S \gamma_S$, where $\alpha_S \geqslant \beta_S \geqslant \gamma_S$ are the three eigenvalues of s_{ij} arranged in descending order. Incompressibility implies $\alpha_S + \beta_S + \gamma_S = 0$. Thus, $R > 0$ with $Q \ll 0$ requires $\alpha_S, \beta_S > 0$ and $\gamma_S < 0$ associated with a sheetlike local flow topology, while $R < 0$ arises when there is only a single stretching axis ($\alpha_S > 0$), i.e., a tubelike topology.

The invariants are inherently rich in physical information regarding both the flow topology and the enstrophy dynamics, and have been widely used to describe the dynamics of turbulent flows [25–28]. In particular, the joint probability density function (PDF) of Q and R unites the main features of turbulence into a single plot exhibiting a universal "teardrop" shape which is present in virtually all turbulent flows [16,25–27]: it displays a clear (anti)correlation between Q and R in the region ($Q < 0, R > 0$) associated with a sheetlike structure, and in the region ($Q > 0, R < 0$) associated with a predominance of vortex stretching over compression [e.g., Fig. 5(d)]. However, it has been stressed that the invariants only provide "local" information and are unable to describe any sort of coherent structure, which by definition requires information from a set of different flow points. Nevertheless, there have been numerous attempts to connect large-scale flow structures to the information of the invariants [29].

It has been shown that the teardrop shape is not present in the non-turbulent region, but as the fluid particles are entrained into the turbulent region, the teardrop forms remarkably fast, requiring a distance of only one Taylor microscale from the non-turbulent region to form completely at the edge of a jet [24,30]. Yet the steps in its formation remain largely ignored. The formation of the teardrop

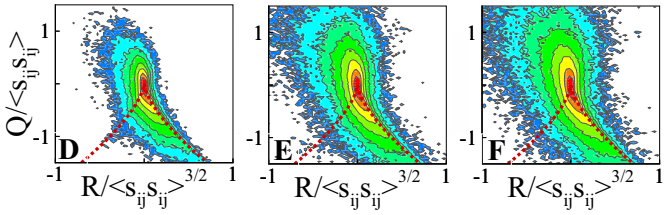

FIG. 5. Joint probability density function of Q and R across the TSL region in the flow: point of zero diffusion (D), point of minimum diffusion (E), and point of maximum enstrophy (F).

shape across the TNTI is analyzed here for the first time, by plotting the joint PDFs of Q and R at several fixed distances from the TNTI layer. Figure 4 shows the PDFs in the VSL [at $y_I/\eta = 0$ (A), -2.4 (B), and -3.1 (C)], while Fig. 5 shows the PDFs in the TSL [at $y_I/\eta = -3.9$ (D), -5.5 (E), and -6.3 (F)]. The VSL is predominantly responsible for the formation of the teardrop shape in the fourth quadrant, associated with a predominance of sheet structures, because $\omega_i \approx 0$ inside the VSL yields $Q \approx -s_{ij}s_{ij}/2 < 0$ and $R \approx -\alpha_S\beta_S\gamma_S$. Since the VSL is at the edge of the eddies from the turbulent region [17], strain dominates over enstrophy, and $R > 0$ (sheet structures) is more frequent than $R < 0$ (tube structures). In contrast, the formation of the teardrop shape in the TSL occurs in the second quadrant with the enstrophy now overcoming strain, thus $Q \approx \omega_i\omega_i/4 > 0$ and $R \approx -\omega_i\omega_j s_{ij}/4$. The predominance of the vorticity over the strain in the flow implies that the enstrophy can grow when ω_i and s_{ij} are correlated so that $\omega_i\omega_j s_{ij} > 0$, i.e., more frequent events of $R < 0$ (vortex stretching) than $R > 0$ (vortex compression). The increasing intensity of Q and R as one moves from A to F naturally reflects the increasing intensity of the fluctuating fields of enstrophy and strain. The results are in agreement with the conditional profiles displayed in Fig. 3. It is noteworthy that in contrast with the jet (where the teardrop forms in $\langle\delta_\omega\rangle \sim \lambda$), the thickness of the TSL is $\langle\delta_\omega\rangle \sim \eta$, and the teardrop shape forms in a much shorter distance, requiring only $\approx -5.5\eta$ to form completely. Indeed, the joint PDF of (Q, R) at E is virtually identical to F and also G (not shown). A very interesting perspective of the formation of the teardrop is provided by the trajectory of the (conditional average of the) invariants of the velocity gradient tensor in the Q-R map, obtained from the conditional mean profiles using the three different orientations (1D, 2D, and 3D), presented in Fig. 6. Only in the second quadrant, we observe some differences in the statistics,

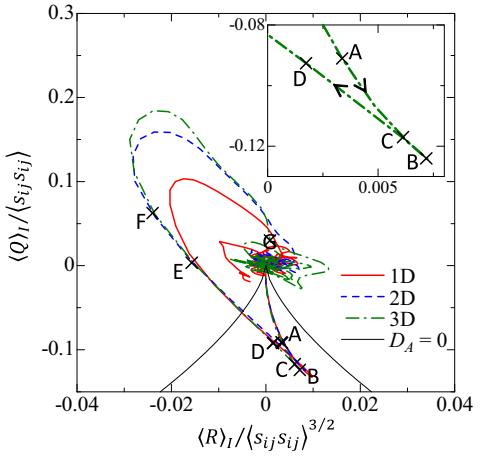

FIG. 6. Trajectory of the conditional mean values of Q and R across the TNTI layer. $D_A = 27/4R^2 + Q^3$ is the discriminant of the eigenvalues of A_{ij}.

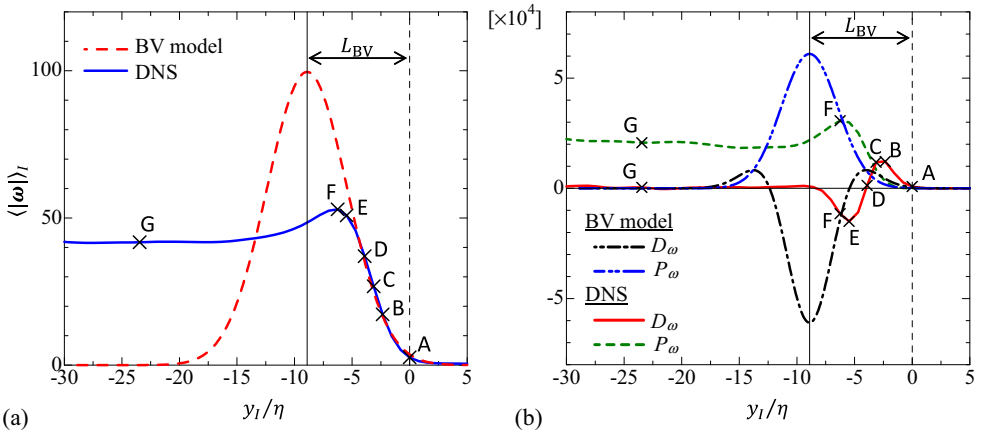

FIG. 7. Conditional mean profiles of (a) vorticity magnitude $|\boldsymbol{\omega}|$ and (b) enstrophy production (P_ω) and enstrophy viscous diffusion (D_ω) obtained from the DNS compared with the results from the BV model. The vertical lines represent the locations of the irrotational boundary (dashed) and the BV axis (solid).

which shows the robustness of the conditional statistics. The non-turbulent region and the VSL are represented only in the fourth quadrant, while the TSL develops in the third quadrant, with some points appearing in the second quadrant. The turbulent core region is mainly in the second but also in the first quadrant. There is an increasing tendency for generating a sheet topology as the fluid particles enter the VSL (A to C), followed by a sharply increased predominance of vortex stretching and formation of tube structures as the flow evolves inside the TSL (C to F), in agreement with the model for the VSL proposed in Ref. [17]. Interestingly, the trajectory connecting the VSL and TSL regions (B to E) consists of a straight line with a constant slope which is the same for all the three orientations used in the conditional statistics (1D, 2D, and 3D). As we see below, this trajectory is a direct manifestation of the presence of intense vortices near the TNTI.

V. COMPARISON OF THE VORTICITY MODEL WITH RESULTS FROM DNS

In this section, the analytical results derived from the BV model are compared with the DNS results. This requires the determination of the several model parameters, which we obtain directly from the reference DNS. The Appendix details how these quantities were estimated from the DNS. Specifically, we use $\nu = 0.003$ while α is estimated by assuming $R_{BV} = 4.9\eta$, and Γ_0 is computed assuming a circulation Reynolds number equal to $\mathrm{Re}_\Gamma = \Gamma_0/\nu = 19.0\mathrm{Re}_\lambda^{1/2}$. Finally, L_{BV} is computed as the sum of the radius of the BV and the mean VSL thickness, in agreement with Eq. (16), leading to $L_{BV} = R_{BV} + \delta_\nu = 4.9\eta + 4\eta = 8.9\eta$, where $\delta_\nu = 4\eta$ is the typical value reported by the DNS [12,17]. Here, the comparison is limited to the simple conditional statistics since the BV model considers the IB defined at one point on an r-θ plane. The BV model cannot be used for studying the relation between the TNTI geometry and the detailed vortex structure underneath the TNTI. The statistics in the DNS are calculated using a coordinate system taken in the normal direction to the IB, while the coordinate direction crossing the vortex center is used in the BV model. In previous DNS studies, a large number of tubelike vortex structures were observed underneath the TNTI [11], and it is inferred that the probability that we find tubelike vortex structures on the local coordinate system is very high. This justifies the present comparison between the conditional statistics and the BV model.

We start with the conditional averages of vorticity magnitude, enstrophy production, and enstrophy diffusion, which exhibit the well-known characteristic shape described in relation to Fig. 3. For clarity, the comparison is split into two figures, where Fig. 7(a) shows the conditional vorticity magnitude profile while Fig. 7(b) shows the conditional enstrophy production and diffusion. The BV

model agrees very well with the DNS near the irrotational boundary until about $y_I/\eta = -3.9$ (D), which is close to the end of the VSL. This is true for the vorticity magnitude as for its production and viscous diffusion. Specifically, the enstrophy profile displays a very similar shape and agrees with the exact location of the DNS curve from the irrotational boundary until the start of the TSL (end of the VSL), which is located at $y_I/\eta = -3.9$ (D). Similarly, the modeled enstrophy production P_ω and viscous diffusion D_ω profiles are very similar to the ones obtained in the DNS, provided the results are taken from the VSL (A to C). The exact locations for the enstrophy production and viscous diffusion in the DNS are not captured from the BV model, but the "shift" is equal to only 1η or less, which is very small indeed. The fact that the enstrophy diffusion peak is captured (B) is particularly impressive. Indeed, the agreement inside the whole VSL (A to C) is remarkable considering the simplicity of the model. The small discrepancies observed here are possibly explained by the strain field, which is assumed to be constant in the BV model, while the effective strain acting on the vortices decreases near the TNTI [11] (see also the Appendix). Moreover, the effects of the other interacting eddies are not accounted for in the BV model and will tend to increase the actual diffusion near the TNTI. Furthermore, the small-scale incoherent strain (supposedly small but non-zero) in the VSL is also not accounted for in the BV model.

After this region, when moving into the TSL (D to G) the results generally diverge, with the enstrophy and enstrophy production term from the BV model tending to zero while they tend to the turbulent core value in the DNS (for the enstrophy and enstrophy production). The weak agreement between the BV model and the DNS in the TSL and in the turbulent core region (D to G) is not surprising, because the number of intense vortices greatly increases in these regions and they are not particularly aligned to the interface tangent [11]. Moreover, the strong non-linearity of the turbulence, resulting from the complex interactions between strain and vorticity described before in relation to Figs. 4 and 5, produces a very complex small-scale field which is incompatible with the simple description given by the BV model. This explains why the results from the BV model cannot be compared or used to predict the joint PDFs of Q and R. Indeed, as described before in Eq. (8), Q and R are described by a simple linear relationship for a BV, and thus for given vortex characteristics, each radial coordinate point r in the vortex is represented by a single straight line in the Q-R map, with $Q(r) \sim -R(r)/\alpha$. A collection of several eddy types can hardly fill in the entire Q-R map, particularly if these eddies have very similar characteristics, such as the same core radius with $4.5 \leqslant R_{\mathrm{BV}} \leqslant 5.5$ [11].

However, it is probably possible to explain part of the results observed in the Q-R map described in Fig. 6. Recalling that a small-scale eddy has a vortex core radius equal to $R_{\mathrm{BV}}/\eta \approx 4.5$ [22], the time scale of the strain rate imposed on this eddy can be estimated with the BV as $1/\alpha = (4\nu/R_{\mathrm{BV}}^2)^{-1} \approx 5.1\tau_\eta$ [$\tau_\eta = (\nu/\varepsilon)^{1/2}$ is the Kolmogorov time scale]. On the other hand, by measuring the slope of the straight line in the (Q,R) trajectory from B to E with the relation $Q(r) \sim -R(r)/\alpha$ (Fig. 6), we arrive at the time scale of the stretching rate of $1/\alpha \approx 5.5\tau_\eta$, which is remarkably close to the value obtained assuming the flow in the VSL and TSL is described by the BV. Thus, the (Q,R) trajectory shows the imprint of the small-scale eddies existing near the TNTI, and unifies the existing models for the VSL and TSL within a TNTI. The small differences obtained with the three orientations in the second quadrant shown in Fig. 6 can now be explained: the 1D orientation is less likely to align with the radial direction of the eddies forming the TNTI than the 3D orientation, which explains why the straight line linking the VSL and TSL is longer for the 3D than for the 1D orientation. Both the teardrop formation and the mean trajectory of (Q,R) are expected to hold for other flows, e.g., fully developed wakes and jets, since the VSL forms at the edge of similar small-scale eddies in these flows [14,17]. However, as described above, the BV model is probably unable to explain the detailed teardrop shape (Fig. 5) because it does not include non-linear effects, e.g., extreme dissipation events ($Q \ll 0$), which tend to occur when two eddies come closer [31].

In order to compare the velocity field related to the entrainment created by the BV model with the one obtained from DNS, Fig. 8 shows a relative streamline through point A in relation to the movement of the irrotational boundary A. Here, we use the velocity field relative to the irrotational boundary (enstrophy isosurface) movement, $\Delta\mathbf{U}$, since the conventional streamline

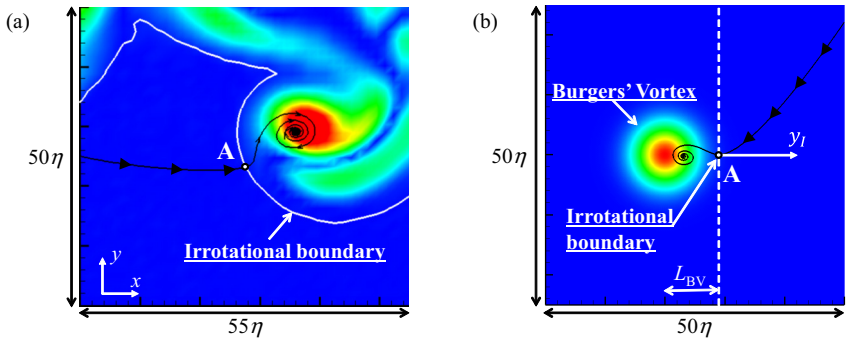

FIG. 8. A single streamline in relation to a point (A) located at the irrotational boundary on a two-dimensional plane perpendicular to the axis of a nearby vortex near the TNTI (a) in the DNS and (b) in the BV model. These streamlines are defined by the velocity field relative to the velocity of the enstrophy isosurface at point A. Point A corresponds (as in the rest of the paper) to the irrotational boundary location close to the vortex location, while the color contours represent $|\omega_z|$, with red and blue corresponding to high and low values, respectively.

shows the convection of the TNTI rather than the entrainment velocity [32]. In contrast, the relative velocity describes well the movement of fluid particles being entrained within the TNTI layer [10]. It is important to understand that the peculiar shape of these streamlines results precisely from the "relative" velocity being computed in relation to a given position outside the axis of the nearby vortex. This explains why these streamlines are very different from the classical circular streamlines observed around the axis of a vortex. The particular location used in Fig. 8(a) was chosen to capture one of the strong eddies lying near the TNTI.

Far away from point A in the non-turbulent region (or for $y_I > 0$) the streamline is smooth and approaches point A, and once the streamline crosses the irrotational boundary (at point A) it moves away from the y_I axis and spirals toward a point located at the edge of the vortex (not at its axis). This trend is very similar in both figures, and the detail of the streamline of $\Delta\mathbf{U}$ around the actual eddy observed in the DNS is similar to the one near the BV. This comparison suggests that the BV model could be useful to describe the instantaneous entrainment processes near the TNTI associated with the small-scale eddy structures. The fluid particle movement within the TNTI layer during the entrainment was recently studied in free shear flows [10]. It was shown that once the particles cross the irrotational boundary, within the viscous superlayer, the particles move in the direction normal to the irrotational boundary. Shortly after this, once the particles reach the turbulent sublayer, they move in the tangential direction to the irrotational boundary. It was also found that while the particles are moving within the TNTI layer, they tend to circumvent the vortex core regions of the intense nearby eddies. The instantaneous streamlines of the relative velocity in Fig. 8 also suggest a similar movement of the entrained particles.

In order to quantify the agreement between the actual and modeled entrainment trajectories obtained with the DNS and the BV model, respectively, Fig. 9 displays the joint PDFs of the normal ΔU_N and tangential ΔU_T components of the relative velocity at several distances from the irrotational boundary. Because the tangential component is zero at the irrotational boundary ($y_I = 0$), the normal component at $y_I = 0$ is separately shown at the end of this section as the local entrainment velocity. The results from the analytical BV model are represented with crosses while the DNS results are represented as PDFs to display the scatter of the existing values. Because the relative velocity is related to the entrained fluid movement within the TNTI layer [10], a close inspection of Fig. 9 allows one to understand the trajectory of the entrained fluids in some detail. While ΔU_T is equal to zero right at the irrotational boundary ($y_I/\eta = 0$), ΔU_N has a non-zero value. At the initial stage of the entrainment, the fluid moves in the radial (irrotational boundary normal) direction since the normal component tends to be larger than the tangential component:

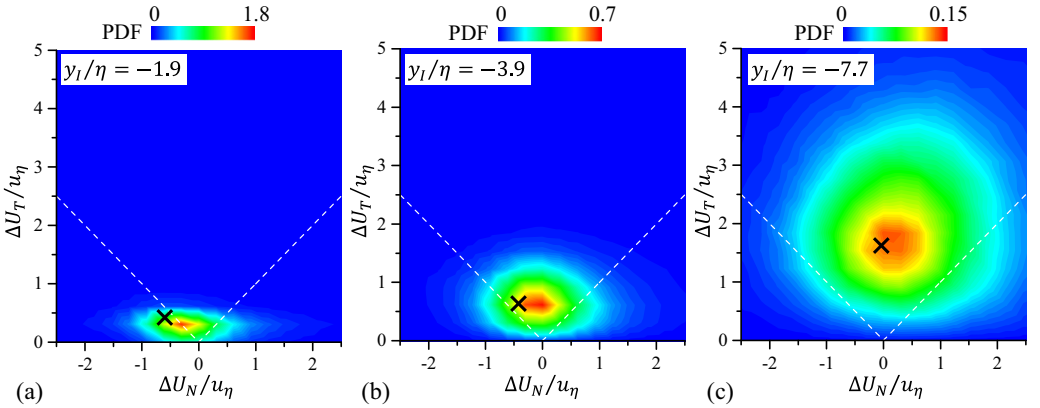

FIG. 9. Joint PDFs of normal and tangential relative velocities, ΔU_N and ΔU_T, respectively, normalized by the Kolmogorov velocity u_η, at several distances from the irrotational boundary, obtained in the DNS. The values of ΔU_N and ΔU_T in the BV model are marked with a cross. The dashed white line represents $\Delta U_T = |\Delta U_N|$.

$|\Delta U_N| > \Delta U_T$. This has been confirmed in the flows with mean shear (turbulent mixing layers [18] as well as in planar jets [10]). However, as the fluid moves into the turbulent region [Figs. 9(a) and 9(b)], the tangential component becomes large: $|\Delta U_N| < \Delta U_T$. It is noteworthy that, already at $y_I/\eta = -7.7$, the tangential component is much larger than the normal component while it is by then quite small [Fig. 9(a)]. Thus, while the fluid motion relative to the irrotational boundary is very slow during the initial stage of the entrainment, it moves much faster in the tangential direction away from the irrotational boundary shortly after the fluid has reached a few Kolmogorov scales inside the TNTI layer. Clearly the values for the BV model are very close to the DNS results provided we are inside the VSL ($-3.9 \leqslant y_I/\eta \leqslant 0$). This is attested to by the very small distance between the peak of the PDFs and the cross representing the BV results, where this difference is much smaller than u_η. Even at $y_I/\eta = -7.7$ [Fig. 9(c)] the agreement between the relative velocity given by the BV model and the peaks of the PDFs obtained from the DNS data is fairly good. In any case, the exact value of the relative velocity obtained by the BV model is close to the peaks of maximum probability computed from the DNS, and the description of the entrainment trajectory given by the BV model agrees with the Lagrangian movement of fluid particles [10,19], which again shows that the isolated eddy modeled by the BV provides an accurate representation of the fluid motion within the TNTI layer.

As described by the BV model in the form of Eqs. (14) and (15), the normal and tangential components of the relative velocity are related to the irrotational strain and vorticity, respectively; the BV model describes the entrainment across the TNTI layer as two processes: (i) drawing of the non-turbulent fluid toward the vortex core region by the imposed strain, and (ii) advection by the vortex structures, by which the entrained fluid moves away from the irrotational boundary. Note that the velocity induced by the vorticity moves the fluid in the vicinity of the TNTI toward the turbulent-core region, because away from the y_I axis the velocity induced by the vorticity points toward the turbulent-core region. The BV model captures well the two stages of the entrainment process: the initial movement of the entrained fluid in the irrotational boundary normal direction and the tangential movement from a few Kolmogorov length scales inside the irrotational boundary, which have been found in the Lagrangian statistics of the distance between the entrained fluid particle and the irrotational boundary [10].

Arguably, the large-scale flow features impose the entrainment rate by acting on the strain rate field, since the strain acting on the worms observed in turbulent flows is related to the integral scale [22]; however, the vorticity of the worms themselves is clearly associated with the smallest

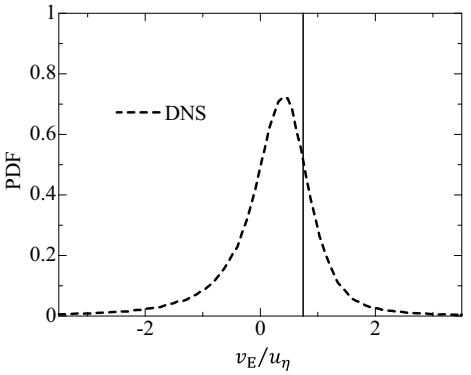

FIG. 10. Probability density function of the local entrainment velocity v_E obtained from the DNS compared with the value in the BV model represented by the solid line ($v_E/u_\eta = 0.75$). The velocities are normalized by the Kolmogorov velocity u_η.

scales of motion [22]. Therefore, the interplay between the large and small scales of motion near the TNTI can also be appreciated by analyzing the equations discussed above. For instance, the relative normal velocity is connected with the local entrainment velocity v_E, and both are related to the strain, as strongly suggested by Eqs. (11) and (14). However, it is well known that the local entrainment velocity v_E scales with the Kolmogorov velocity u_η [21], which is clearly a small-scale feature. In the same vein, Eq. (15) links the tangential velocity to the small-scale vorticity field; however, it is well known that the (related) azimuthal velocity of the intense small-scale eddies (worms) is of the order of the root-mean-square velocity, which of course is a large-scale feature [11]. This suggests that the interaction between the several worms near the TNTI could also explain the existing discrepancies between the present BV model and the DNS results; however, the present entrainment model can be extended to include large-scale effects by modeling the strain α (see the Appendix in Ref. [24]), different interface orientations [30], and the external forces such as buoyancy for stably stratified flows at large buoyancy Reynolds number [33], which also act upon the model via the strain imposed on the eddies near the TNTI, thereby affecting the entrainment rate.

Finally, we compare the local entrainment velocity v_E computed from the DNS as Eq. (10) with the one obtained from the BV model, Eq. (11). To allow a detailed comparison of this important quantity Fig. 10 shows the PDF of v_E from the DNS, while the BV model result corresponds to a single value (estimated as described before). The PDF for v_E obtained from DNS seems to be approximately Gaussian, with a range of possible values of the order of the Kolmogorov velocity, while a large probability can be found for positive values of v_E. The negative value of v_E is caused by the viscous dissipation of enstrophy. Note that the inviscid terms in the enstrophy equation are comparatively very small or negligible at the IB position. The peak of the PDF is obtained for $v_E/u_\eta = 0.40$, which agrees very well with the values measured by Wolf *et al.* [21]. For the BV model we get $v_E/u_\eta = 0.75$, which is very close to the DNS values, considering the simplicity of the present model.

VI. CONCLUSIONS

The dynamics of the flow near TNTIs in SFT is compared with a single eddy placed near an irrotational boundary. The DNS used in this study attains the turbulent Reynolds number $\mathrm{Re}_\lambda \approx 100$, and conditional statistics are computed in relation to the irrotational boundary position, while the single eddy is modeled using a steady BV model, which has only three parameters: the kinematic viscosity of the fluid, ν, the strain rate acting on the vortex, α, and the vortex circulation Γ_0. These parameters are taken from the intense vorticity structures (worms) near the TNTI layer as obtained from DNS. The BV model underlines a distinction between the velocity field associated with the

irrotational strain and the vorticity near a single vortex. While the strain imposed on the vortex draws non-turbulent fluid toward the vortex core region, the motion induced by the vorticity moves the entrained fluid into the turbulent-core region.

The analytical results for the BV model predict reasonably well the conditional profiles of enstrophy, enstrophy production, and enstrophy diffusion within the TNTI layer. Specifically, the quantities are well captured inside the VSL and not inside the TSL. The formation of the teardrop shape of the joint PDF of Q and R is analyzed inside the VSL and TSL in detail using the DNS, and the different nature of the two layers is clearly illustrated. Moreover, it turns out that inside these two layers, the invariants Q and R show the imprint of the small-scale eddies or worms from the turbulent core region, thus providing a remarkable example where local flow topology and dynamics are intertwined to the spatial coherence of the flow. Furthermore, the simple BV model is able to capture these features. The streamline of the flow relative to the irrotational boundary movement near the TNTI obtained from an intense eddy captured from the DNS is well reproduced by the present BV model, both qualitatively and quantitatively, and finally the entrainment velocity of the fluid within the TNTI layer is reasonably well estimated from the BV model. Thus the main features of the entrainment mechanism are well reproduced.

The way that the effects arising from the large and the small scales of motion can be accounted for in the model are briefly discussed, as well some of its limitations. In its present form, the model misses the effects that result from the interactions of several similar vortices near the TNTI layer as well as from any small-scale incoherent vorticity existing in the flow, which certainly play a more crucial role inside the TSL and turbulent-core regions. The model can be extended to cover these limitations and to describe several different flows and provides an interesting framework to understand the entrainment mechanisms associated with the small-scale nibbling mechanism.

ACKNOWLEDGMENTS

This work was partially supported by the "Collaborative Research Project on Computer Science with High-Performance Computing in Nagoya University" and by JSPS KAKENHI Grants No. 25002531, No. 25289030, No. 25289031, and No. 16K18013. C.B.d.S. acknowledges Fundação para a ciência e Tecnologia (FCT), under Grant No. PTDC/EMS-ENE/6129/2014.

APPENDIX

This Appendix describes how the parameters for the BV model were obtained from the DNS of SFT. We use the vortex tracking algorithm described in Ref. [11], where each one of the IVSs or worms is tracked and its characteristics are computed in relation to the irrotational boundary location.

The IVS axis is detected with the points where the vorticity $\omega = |\boldsymbol{\omega}|$ is above a certain threshold ω_{tr}, where this threshold characterizes points with the most intense vorticity existing within the flow domain. We define this threshold as equal to the vorticity of the points with highest enstrophy that are contained in 1% of the total volume. The worm radius R and circulation Γ as a function of axis position are calculated from the vorticity profile along the axis with the same procedure as in Refs. [11,13].

Figure 11 shows the conditional mean vortex radius R for each worm and the circulation Reynolds number Re_Γ as a function of the distance from the irrotational boundary in the SFT. As in Ref. [11], the mean radius is compared with the Burgers vortex radius R_{BV}. These plots are very similar to those in Ref. [11] in terms of magnitudes and shape of the functions. The radius of the worms, R, and the circulation Reynolds number Γ, after being roughly constant inside the turbulent region, increase slightly near the TNTI. However, the radius of the worms is always near the Burgers vortex radius, i.e., $\langle R/R_{\mathrm{BV}}\rangle_I = 1$ throughout the whole range of y_I, implying that the eddies are at all locations in an approximate balance between the enstrophy production and viscous diffusion. As explained in Ref. [11], the slight increase of the worms' characteristics near the TNTI results from

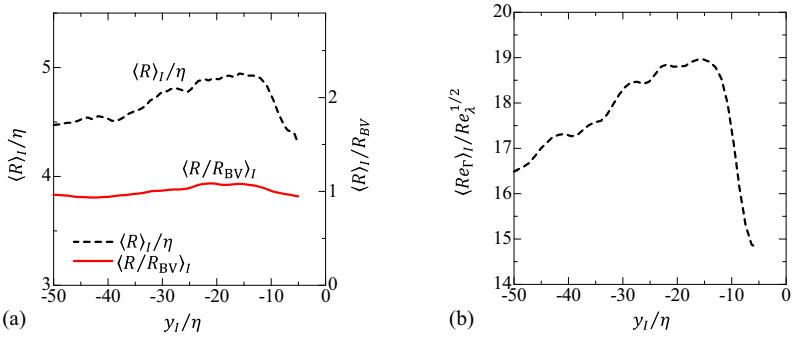

FIG. 11. Conditional mean profiles of (a) core radius R and (b) circulation Reynolds number Re_Γ of the intense vorticity structures or worms, as a function of the distance from the irrotational boundary for the SFT simulation. R is normalized by the Kolmogorov microscale η or by the Burgers vortex radius R_{BV} calculated with the mean stretching rate acting on the worms, while Re_Γ is normalized by the Taylor Reynolds number Re_λ.

the slightly lower strain to which the worms are subjected near the TNTI, compared to inside the turbulent region.

From these figures we take $R_{\mathrm{BV}} = 4.9\eta$ and $\mathrm{Re}_\Gamma = 19.0\mathrm{Re}_\lambda^{1/2}$ at $y_I = -15\eta$. The location of 15η was chosen so that statistics affected by the VSL, whose instantaneous thickness is not constant, are not included in the BV model. With these values we estimate L_{BV} as $L_{\mathrm{BV}} = R_{\mathrm{BV}} + \delta_\nu = 4.9\eta + 4.0\eta = 8.9\eta$. These are then the values used in the BV model assessed in the present work.

[1] C. B. da Silva, J. C. R. Hunt, I. Eames, and J. Westerweel, Interfacial layers between regions of different turbulence intensity, Annu. Rev. Fluid Mech. **46**, 567 (2014).

[2] C. B. da Silva, R. R. Taveira, and G. Borrell, Characteristics of the turbulent/nonturbulent interface in boundary layers, jets and shear-free turbulence, J. Phys. Conf. Ser. **506**, 012015 (2014).

[3] A. Attili, J. C. Cristancho, and F. Bisetti, Statistics of the turbulent/non-turbulent interface in a spatially developing mixing layer, J. Turbul. **15**, 555 (2014).

[4] M. Gampert, J. Boschung, F. Hennig, M. Gauding, and N. Peters, The vorticity versus the scalar criterion for the detection of the turbulent/non-turbulent interface, J. Fluid Mech. **750**, 578 (2014).

[5] G. Borrell and J. Jiménez, Properties of the turbulent/non-turbulent interface in boundary layers, J. Fluid Mech. **801**, 554 (2008).

[6] J. Westerweel, C. Fukushima, J. M. Pedersen, and J. C. R. Hunt, Momentum and scalar transport at the turbulent/non-turbulent interface of a jet, J. Fluid Mech. **631**, 199 (2009).

[7] M. Holzner and B. Lüthi, Laminar Superlayer at the Turbulence Boundary, Phys. Rev. Lett. **106**, 134503 (2011).

[8] K. Chauhan, J. Philip, C. M. da Silva, N. Hutchins, and I. Marusic, The turbulent/non-turbulent interface and entrainment in a boundary layer, J. Fluid Mech. **742**, 119 (2014).

[9] D. Mistry, J. Philip, J. R. Dawson, and I. Marusic, Entrainment at multi-scales across the turbulent/non-turbulent interface in an axisymmetric jet, J. Fluid Mech. **802**, 690 (2016).

[10] T. Watanabe, C. B. da Silva, Y. Sakai, K. Nagata, and T. Hayase, Lagrangian properties of the entrainment across turbulent/non-turbulent interface layers, Phys. Fluids **28**, 031701 (2016).

[11] C. B. da Silva, R. J. N. Dos Reis, and J. C. F. Pereira, The intense vorticity structures near the turbulent/non-turbulent interface in a jet, J. Fluid Mech. **685**, 165 (2011).

[12] R. Jahanbakhshi, N. S. Vaghefi, and C. K. Madnia, Baroclinic vorticity generation near the turbulent/non-turbulent interface in a compressible shear layer, Phys. Fluids **27**, 105105 (2015).

[13] T. Watanabe, C. B. da Silva, K. Nagata, and Y. Sakai, Geometrical aspects of turbulent/non-turbulent interfaces with and without mean shear, Phys. Fluids **29**, 085105 (2017).
[14] J. Philip and I. Marusic, Large-scale eddies and their role in entrainment in turbulent jets and wakes, Phys. Fluids **24**, 055108 (2012).
[15] M. A. C. Teixeira and C. B. da Silva, Turbulence dynamics near a turbulent/non-turbulent interface, J. Fluid Mech. **695**, 257 (2012).
[16] P. A. Davidson, *Turbulence: An Introduction for Scientists and Engineers* (Oxford University Press, Oxford, U.K., 2004).
[17] R. R. Taveira and C. B. da Silva, Characteristics of the viscous superlayer in shear free turbulence and in planar turbulent jets, Phys. Fluids **26**, 021702 (2014).
[18] T. Watanabe, Y. Sakai, K. Nagata, Y. Ito, and T. Hayase, Turbulent mixing of passive scalar near turbulent and non-turbulent interface in mixing layers, Phys. Fluids **27**, 085109 (2015).
[19] R. R. Taveira, J. S. Diogo, D. C. Lopes, and C. B. da Silva, Lagrangian statistics across the turbulent-nonturbulent interface in a turbulent plane jet, Phys. Rev. E **88**, 043001 (2013).
[20] T. Watanabe, Y. Sakai, K. Nagata, Y. Ito, and T. Hayase, Enstrophy and passive scalar transport near the turbulent/non-turbulent interface in a turbulent planar jet flow, Phys. Fluids **26**, 105103 (2014).
[21] M. Wolf, M. Holzner, B. Lüthi, D. Krug, W. Kinzelbach, and A. Tsinober, Effects of mean shear on the local turbulent entrainment process, J. Fluid Mech. **731**, 95 (2013).
[22] J. Jimenez and A. A. Wray, On the characteristics of vortex filaments in isotropic turbulence, J. Fluid Mech. **373**, 255 (1998).
[23] A. Vincent and M. Meneguzzi, The dynamics of vorticity tubes in homogeneous turbulence, J. Fluid Mech. **258**, 245 (1994).
[24] C. B. da Silva and J. C. F. Pereira, Invariants of the velocity-gradient, rate-of-strain, and rate-of-rotation tensors across the turbulent/nonturbulent interface in jets, Phys. Fluids **20**, 055101 (2008).
[25] J. Martín, A. Ooi, M. S. Chong, and J. Soria, Dynamics of the velocity gradient tensor invariants in isotropic turbulence, Phys. Fluids **10**, 2336 (1998).
[26] J. Soria, R. Sondergaard, B. J. Cantwell, M. S. Chong, and A. E. Perry, A study of the fine-scale motions of incompressible time-developing mixing layers, Phys. Fluids **6**, 871 (1994).
[27] H. M. Blackburn, N. N. Mansour, and B. J. Cantwell, Topology of fine-scale motions in turbulent channel flow, J. Fluid Mech. **310**, 269 (1996).
[28] J. Soria, A. Ooi, and M. S. Chong, Volume integrals of the Q_A-R_A invariants of the velocity gradient tensor in incompressible flows, Fluid Dyn. Res. **19**, 219 (1997).
[29] G. E. Elsinga and I. Marusic, Universal aspects of small-scale motions in turbulence, J. Fluid Mech. **662**, 514 (2010).
[30] T. Watanabe, Y. Sakai, K. Nagata, Y. Ito, and T. Hayase, Vortex stretching and compression near the turbulent/nonturbulent interface in a planar jet, J. Fluid Mech. **758**, 754 (2014).
[31] B. Ganapathisubramani, K. Lakshminarasimhan, and N. T. Clemens, Investigation of three-dimensional structure of fine scales in a turbulent jet by using cinematographic stereoscopic particle image velocimetry, J. Fluid Mech. **598**, 141 (2008).
[32] J. Philip, I. Bermejo-Moreno, D. Chung, and I. Marusic, Characteristics of the entrainment velocity in a developing wake, in *Proceedings of the Ninth International Symposium on Turbulence and Shear Flow Phenomena (TSFP-9), Melbourne, Australia* (University of Melbourne, 2015), Vol, 3, paper 9C-5.
[33] T. Watanabe, J. J. Riley, and K. Nagata, Effects of stable stratification on turbulent/nonturbulent interfaces in turbulent mixing layers, Phys. Rev. Fluids **1**, 044301 (2016).